nature communications

Article

https://doi.org/10.1038/s41467-026-74708-3

Portable, real-time 3D ultrasound for operator-independent breast imaging

Received: 16 February 2026

Accepted: 14 June 2026

Published online: 01 July 2026

Check for updates

Md Osman Goni Nayeem[1,4], Shrihari Viswanath[1,4], Hyeokjun Yoon[1,4], Aastha Shah[1], David Sadat[1], Colin Marcus[1,2], Anantha P. Chandrakasan[2], Tolga Ozmen[3] & Canan Dagdeviren[1]

Breast cancer screening and longitudinal monitoring require imaging technologies that are portable, operator-independent, and suitable for frequent use, a capability not fully met by mammography or conventional ultrasound. We present a three-dimensional (3D) portable ultrasound system for real-time examination (3D PURE) that overcomes key limitations in volumetric breast imaging through advances in transducer design, acoustic materials, and adaptive beamforming. A box-array design incorporating a corner-gap offset geometry suppresses peak crosstalk (by 3.73 dB at the corner-most element), prevents preamplifier saturation, and supports higher transmit voltages (up to 24 V). A custom flowable backing layer (impedance 6.12 MRayl; attenuation 7.56 dB mm^{-1} MHz^{-1}) integrates around fragile wirebonds, reduces inter-element crosstalk by ~4.5 dB throughout the array, and improves axial and lateral/elevational resolutions by ~200 μm and ~70 μm, respectively. Layered Aberration-Correction Reconstruction (LACR), an adaptive 3D beamformer, compensates for heterogeneous speed-of-sound (SoS) in the breast, reducing depth localization error by 2 mm and aberration defocusing by 70 μm on average at a 5 cm depth. Nine of the ten participants in an in vitro study showed improved microtarget detection efficiency with 3D PURE relative to a conventional 2D system ($p = 0.0215$), analogous to detection of microcalcifications. These results, combined with in vivo imaging validation of various phenotypes, highlight the potential of 3D PURE for reliable breast imaging. Furthermore, a vision-guided computer interface, MyFUS, ensures self-guided, user-friendly, and operator-independent probe positioning for longitudinal monitoring.

Breast cancer is the most commonly diagnosed cancer worldwide, with an estimated 2.3 million new cases and 670,000 deaths in 2022[1]. Early detection significantly improves survival, with five-year survival exceeding 90% when the disease is diagnosed at a localized stage[2]. Mammography, the current standard for breast cancer screening, has reduced sensitivity in women with dense breast tissue (47–64%)[3], where overlapping tissue can obscure tumors, and cannot be used frequently enough to detect fast-growing interval cancers that arise between scheduled screenings. The requirement for breast compression makes the procedure uncomfortable for many women, and repeated use involves exposure to ionizing radiation, limiting its suitability for frequent monitoring[4]. High cost and infrastructure demand

[1]Media Lab, Massachusetts Institute of Technology, Cambridge, MA, USA. [2]Department of Electrical Engineering and Computer Science, Massachusetts Institute of Technology, Cambridge, MA, USA. [3]Division of Surgical Oncology, Massachusetts General Hospital, Harvard Medical School, Boston, MA, USA. [4]These authors contributed equally: Md Osman Goni Nayeem, Shrihari Viswanath, Hyeokjun Yoon. e-mail: canand@media.mit.edu

further restricts its availability, especially in low-resource settings[5]. Early breast anomalies can undergo clinically meaningful changes over time, underscoring the need for longitudinal monitoring approaches[6].

Alternative modalities such as magnetic resonance imaging (MRI)[7] and molecular breast imaging (MBI)[8] offer high sensitivity but are constrained by higher cost, long exam times, and, in the case of MBI, radiotracer use and associated radiation exposure[9,10]. These limitations underscore the urgent need for complementary, patient-friendly, and scalable imaging tools that are safe, comfortable, and suitable for frequent longitudinal monitoring. Recent advances in ultrasound technology highlight its potential to fill this gap by providing real-time, radiation-free imaging[11–15], yet current systems remain either highly operator-dependent or cost-prohibitive, limiting their scalability (Supplementary Table 1). Most handheld ultrasound (HHUS) systems capture narrow 2-dimensional (2D) slices (<3 mm) and require careful manual manipulation across the breast, increasing the risk of overlooking anomalies[16], especially microcalcifications,[17] which measure only a few micrometers in size[18]. Automated Breast Ultrasound (ABUS) systems address some of the limitations of handheld systems by standardizing image acquisition and reducing operator variability[19]. However, ABUS systems are bulky, expensive, and typically confined to clinical settings, limiting accessibility and preventing point-of-care or longitudinal use[20]. Our previous report on a real-time 3D ultrasound imaging system addressed several long-standing limitations in volumetric ultrasound by i) achieving portability through an energy-efficient, compact hardware design, and ii) reducing the element count from N^2 to 4 N via a custom box-shaped array architecture, thereby substantially lowering power consumption. This architecture, implemented on a custom printed circuit board (PCB) platform, enabled real-time wide-angle volumetric imaging with minimal computational load. However, the system still faced challenges that limited its translational potential. For instance, backing layers, which are essential for suppressing transducer ringing and improving bandwidth, could not be incorporated because rigid backing materials were mechanically incompatible with fragile gold wirebonds used as interconnects between transducer elements and the electronics. Furthermore, mechanical and electrical crosstalk between neighboring elements degraded image contrast, requiring computational noise-subtraction methods. At higher driving voltages (>18 V), crosstalk led to preamplifier saturation, narrowing the usable operating range. These limitations necessitated a redesigned architecture capable of maintaining low noise and high resolution across a broader voltage range. Additionally, the breast's adipose layer exhibits a lower SoS than glandular tissue, and it varies substantially across individuals. Such variability introduces defocusing in the reconstructed images that must be corrected to achieve high-quality clinical images. In parallel, clinical translation required mitigating operator dependence: although 3D imaging reduces the technical skill required compared with conventional 2D fan-slice imaging, reliable and reproducible monitoring remains critical for consistent coverage and longitudinal monitoring.

In this work, we introduce i) a transducer geometry incorporating a corner-gap offset between adjacent transmit (TX) and receive (RX) elements at the array corners that reduces crosstalk (by 3.73 dB at the corner-most element), preventing amplifier saturation and expanding the operational transmit voltage range (up to 24 V); ii) a backing layer (acoustic impedance: 6.12 MRayl; attenuation: 7.56 dB mm^{-1} MHz^{-1}) that flows around fragile gold wires without damaging them and provides electromagnetic shielding, reducing interelement crosstalk by 4.5 dB on average and enhancing axial resolution by approximately 200 μm and lateral/elevational resolution by roughly 70 μm on average; iii) LACR, an aberration-correction beamformer in a real-time 3D ultrasound imaging system, which enables a reduction in localization error by 2 mm and resolution improvement of over 70 μm on average at 5 cm depth; and iv) a vision interface for operator-independent repetitive monitoring, Mirror my First UltraSound (MyFUS), which integrates body and probe localization to consistently reproduce imaging of the same anatomical region across repeated trials without the need for trained operators. A user study emulating microcalcification screening is carried out to validate the enhanced detectability with less time and cognitive load achieved with 3D PURE. Consistent with the group-level analysis, 90% of the participants showed improved detection efficiency with 3D PURE relative to 2D HHUS (exact sign test, $p = 0.0215$). Additionally, an in vivo study is conducted to image various kinds of phenotypes including microcalcifications, cysts, and solid masses using both a reference clinical ultrasound system and 3D PURE. Together, these advances establish a pathway toward reliable, operator-independent, and real-time 3D ultrasound breast imaging suitable for widespread screening and monitoring, especially in resource-constrained settings.

Results

3D ultrasound imaging system for portable and operator-independent monitoring

A schematic illustration highlights the contrast between the conventional 2D HHUS probe and the proposed 3D PURE (Fig. 1a). The 2D HHUS images a narrow plane and requires rigorous manual repositioning, often resulting in non-uniform sampling and gaps in coverage. In contrast, 3D PURE uses a wide field-of-view (FOV), reducing operator burden and minimizing the number of scans needed to cover the entire breast. The 3D PURE consists of a 128-element box-shaped 2D array, modified from our previous work[12], coupled to an acoustically optimized matching layer and a high-attenuation conductive backing layer that suppresses inter-element crosstalk and electromagnetic interference (EMI). This array is integrated into a compact multilayer electronics stack comprising preamplifiers, transmit electronics, and a custom chirp data acquisition system (cDAQ) (Fig. 1b).

We introduce a flowable conductive backing layer consisting of a high percentage of tungsten (W) and zirconia (ZrO_2) filler in a toluene-diluted polyurethane (PU) polymer matrix, which overcomes the limitation of conventional rigid backing layers that must be individually diced and therefore remain electrically isolated. The flowable backing forms a continuous shielding layer around the elements, improving acoustic attenuation and functioning as EMI shielding (Fig. 1c). The compliant mechanical nature of the PU matrix significantly enhances acoustic damping, reducing ultrasound reverberations more effectively and improving signal fidelity in ultrasound imaging applications.

Breast tissue typically contains a superficial fat layer with a lower SoS than the underlying parenchyma[21]. Conventional assumption of a homogeneous SoS across the entire tissue introduces systematic delay errors that cause echoes to sum incoherently and produce defocusing and localization errors. To address these aberration effects, we incorporated an LACR into our real-time 3D ultrasound system (Fig. 1d).

To further eliminate the operator dependency, we developed a vision interface, MyFUS, designed to facilitate at-home self-monitoring of breast anomalies. MyFUS is a computer vision–based solution that enables patients to reliably reposition the ultrasound probe at the same anatomical location during repeated monitoring. The interface can be operated on any personal computer equipped with a camera, and the procedure consists of two steps: (i) initial probe positioning and (ii) follow-up monitoring (Fig. 1e).

Array geometry and ZrO_2-W–based polymer backing layer

To expand the operational transmit voltage range and to reduce the crosstalk, we adapted a transducer array geometry with corner-gap offsets and an attenuative, flowable and conducting backing layer (Fig. 2a). In conventional box arrays[12], the corner elements suffer from maximum crosstalk which limits the maximum operating voltage due to preamplifier saturation. To mitigate this effect, we introduced an

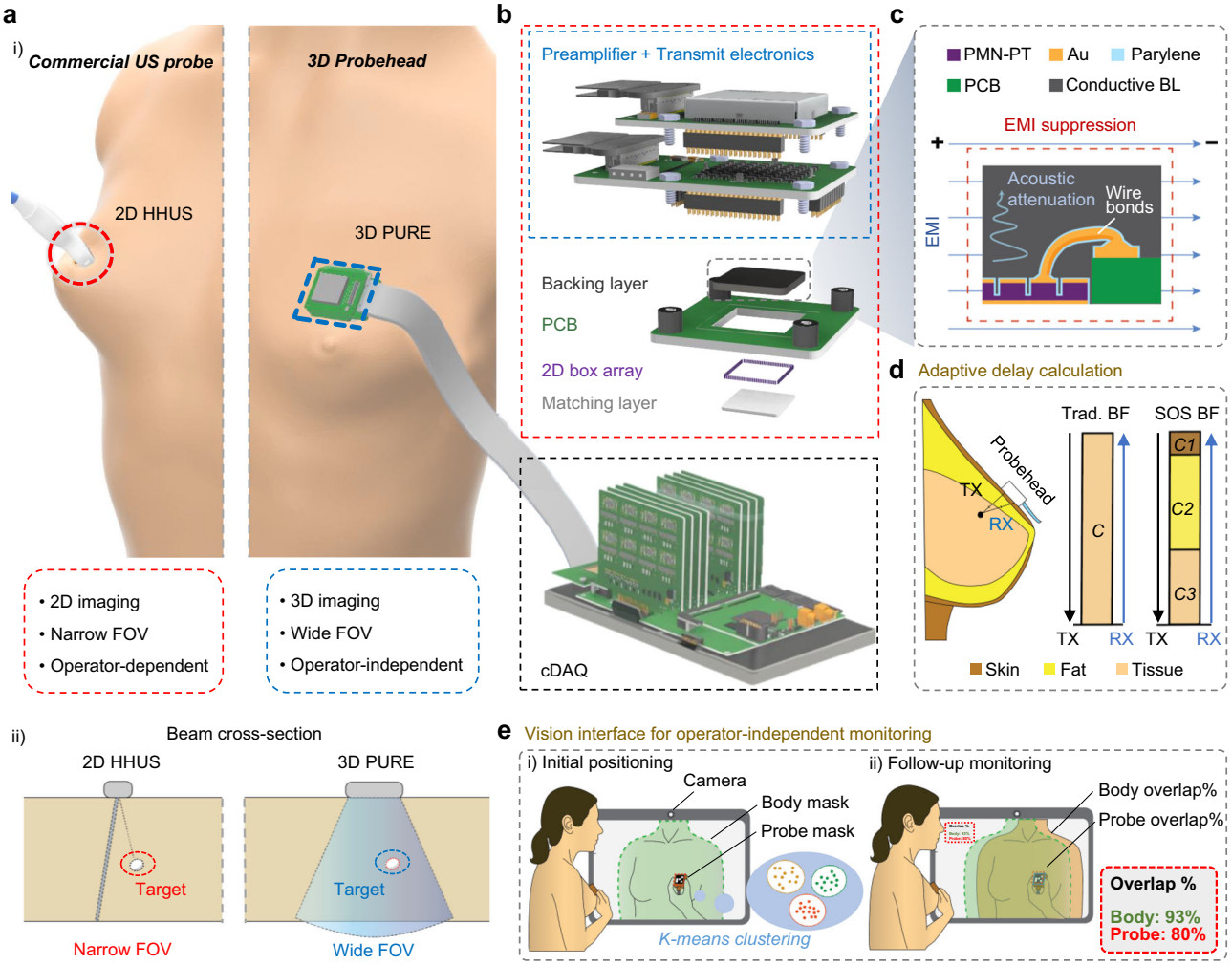

Fig. 1 | Overview of the 3D portable ultrasound for real-time examination (PURE) for portable and operator-independent monitoring. a Overview of the portable 3D PURE probehead for 3D ultrasound breast imaging with wider field-of-view (FOV) in comparison to the conventional 2D hand-held ultrasound (HHUS) probe. **b** Device layout for each component of the 3D PURE probehead and a custom chirped data acquisition system (cDAQ). **c** Schematic of the backing layer (BL) on the piezoelectric material layer, which also covers the wirebonding which connects the piezoelectric material to the electrode pad on the carrier printed circuit board (PCB). The conductive backing layer enables not only the conventional acoustic attenuation, but also the shielding effect to reduce the electromagnetic interference (EMI). **d** Schematic illustration showing the adaptive delay calculation and the layered model for the aberration-correction beamformer (BF). Transmit (TX) and receive (RX) delays are accurately estimated according to the speed of sound (*C*) of each anatomical layer. **e** A vision interface for self-probe repositioning by patients themselves for repetitive and longitudinal monitoring of the breast at home.

offset between adjacent corner-element pairs, reducing high frequency (HF) crosstalk (Methods) by 3.73 dB between corner elements compared to the case without the offset from −16.96 to −20.69 dB (Fig. 2c, Methods). This modification enables stable operation at higher voltages, increasing the operating limit to 24 V compared to the original 18 V without the offset. At this setting, crosstalk at the corner element remained below the preamplifier's saturation threshold, ensuring reliable operation at a higher voltage. Among the various design patterns evaluated to increase spacing between corner elements, our corner-gap offset configuration provides the best balance between increased element distance and point spread function (PSF) degradation (Supplementary Fig. 1). Finite Element Analysis (FEA) indicates a 9.12 dB reduction in structural mechanical coupling (Supplementary Figs. 2,3, Supplementary Note 1), with the observed 3.73 dB experimental improvement representing the total system response as constrained by the residual electronic crosstalk.

To enhance imaging performance and further mitigate electronic crosstalk, we developed a backing layer composed of a PU–based polymer matrix filled with W and ZrO_2 microparticle fillers. The mixture is diluted in toluene so that it can flow over the fragile gold wire interconnects during the lamination, and it subsequently solidifies upon solvent evaporation (Supplementary Fig. 4). This process enables dicing-free post-lamination of the backing layer, after initial laser-micromachining of array elements and gold wire bonding (Supplementary Fig. 5). It minimizes the risk of mechanical damage to delicate piezoelectric ceramics and wire bonds (Supplementary Fig. 6) while conventional mechanical dicing often induces cracking and damage in brittle PMN–PT[22], especially during full-stack dicing. This substantially enhances process reliability and enables a fabrication yield close to 100%.

PU is selected as the polymer matrix for composite backing layer due to its intrinsically high acoustic attenuation[23]. The viscoelastic nature of PU, imparted by its flexible polymer chains, enables significant mechanical and acoustic energy dissipation through inertial friction and molecular relaxation mechanisms within the polymer network[24]. This characteristic provides superior damping performance compared to conventional epoxy-based materials typically used in backing layers[25–28]. With a fixed amount of PU and toluene, we varied the ZrO_2-W ratio to achieve an optimized backing layer composite with high attenuation while maintaining sufficient acoustic impedance. The

https://doi.org/10.1038/s41467-026-74708-3

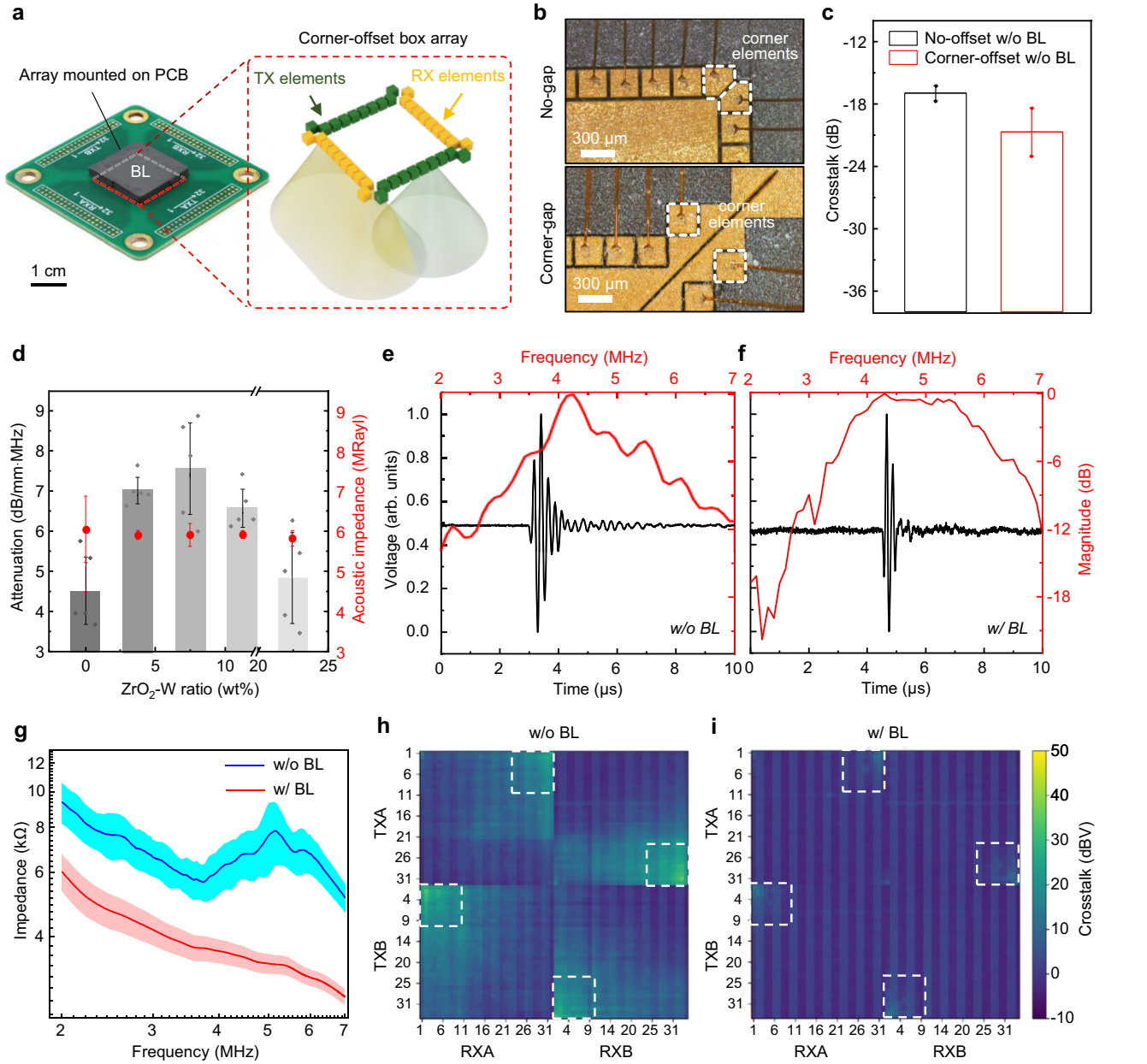

Fig. 2 | Characterization of the ultrasound transducer array and backing layer. **a** Photograph of the probehead with a backing layer. Under the BL, piezoelectric elements in a form of corner-gap offset box array are connected to the carrier PCB. **b** Photographs of the no-gap corner element structure and the corner-gap corner element structure. **c** Crosstalk magnitude between one TX corner element and two proximal RX corner elements, without (w/o) the BL (No-gap -16.96 ± 0.71 dB vs Corner-gap -20.69 ± 2.31 dB) ($n = 2$, corner pairs). **d** Attenuation coefficient and acoustic impedance of the BL with different weight ratio (wt%) of ZrO_2-W composition. Attenuation (dB mm^{-1} MHz^{-1}): 4.55 ± 0.84, 7.03 ± 0.33, 7.56 ± 1.14, 6.58 ± 0.47, and 4.83 ± 1.02 from left to right. Acoustic impedance (Mrayl): 6.25 ± 0.76, 6.12 ± 0.10, 6.12 ± 0.26, 6.13 ± 0.09, and 6.04 ± 0.18 from left to right ($n = 5$, samples). **e** Impulse-response and bandwidth plot of the device w/o the BL. **f** Impulse-response and bandwidth plot of the device with (w/) the BL. **g** Electrical impedance of the element within a device. Average and standard deviation values were calculated between 64 elements from one pair of TX and RX rows in the same device, w/o and w/ the BL. **h** Channel-wise crosstalk magnitude map between TX and RX elements w/o the BL. **i** Channel-wise crosstalk magnitude map between TX and RX elements w/ the BL (TXA: TX element 1-32, TXB: TX element 33-64, RXA: RX element 1-32, and RXB: RX element 33-64). Element pairs near the corner were marked with white dotted boxes. Scale bars: 1 cm (**a**) and 300 μm (**b**).

W loading fraction was optimized to maximize acoustic impedance while maintaining adequate mixing and processability with the polymer matrix (Supplementary Fig. 7). In particle-loaded polymer backings, acoustic attenuation arises predominantly from scattering and absorption at the filler–matrix interfaces[23,29]. Within the composite, ZrO_2 microparticles serve as high-impedance scatterers within the polymer matrix, analogous to other heavy-oxide fillers[30]. Their inclusion enhances multiple scattering and interfacial losses, thereby increasing the composite's effective attenuation. Acoustic attenuation was measured across composites with varying ZrO_2–W ratios (Supplementary Fig. 8). The formulation containing 7.5 wt% ZrO_2 exhibited the highest attenuation of 7.56 ± 1.14 dB mm^{-1} MHz^{-1} ($n = 5$) (Fig. 2d). Increasing the ZrO_2-W ratio into the composite produced a slight reduction in the acoustic impedance from 6.25 ± 0.76 MRayl (0 wt% ZrO_2-W composite) to 6.04 ± 0.18 MRayl (22.5 wt% ZrO_2-W composite), which has negligible effect on the acoustic matching. Owing to its high attenuation while maintaining favorable acoustic impedance (6.12 ± 0.26 MRayl), the composite containing 7.5 wt% ZrO_2-W was

selected as the optimized formulation for the backing layer. The final backing layer containing 7.5 wt% ZrO_2–W exhibits a superior attenuation coefficient compared with most reported backing materials, except for designs using saturated tungsten loading in polyurethane[23] or hot-pressed backing layers fabricated under high pressure and temperature[31]. However, saturated tungsten composites are incompatible with fragile wire-bond interconnects due to their high viscosity, while hot-press processes may degrade the performance of piezoceramics and break wire bonds in our fabrication workflow (Supplementary Table 2).

The addition of the backing layer to the array reduces the ringing, where the signal from the element with the backing layer exhibits a shorter decay time compared to the element without it (Fig. 2e, f). Consequently, the −3 dB bandwidth increased from 0.63 MHz (3.94–4.57 MHz) to 2.24 MHz (3.68–5.92 MHz), and the −6 dB bandwidth expanded from 2.23 MHz (3.44–5.67 MHz) to 3.10 MHz (3.42–6.52 MHz). The averaged resonance and anti-resonance frequencies of individual array elements are 3.75 MHz and 5.14 MHz ($n = 64$), corresponding to electrical impedances of 5.65 kΩ and 7.8 kΩ, respectively (Fig. 2g). The backing layer reduced the overall electrical impedance, bringing the impedance at 3.75 MHz down to 3.72 kΩ. This reduction is attributed to the enhanced acoustic energy absorption by the backing layer, which effectively damps mechanical ringing. The results were further validated through FEA simulations, which demonstrate reduced ringing in the acoustic pressure response and an increased bandwidth (Supplementary Note 2, and Supplementary Figs. 9,10). The simulated −6 dB bandwidth of the transducer without the BL ranged from 3.771 MHz to 5.103 MHz, and the addition of the BL expanded the −6 dB bandwidth to 3.607–6.659 MHz, closely matching the experimental results.

In addition, owing to the high W content, the developed backing layer exhibits an electrical conductivity of 0.3933 S m^{-1} (Supplementary Fig. 11). This polymer composite thus helps reduce electromagnetic coupling between channels, complementing its primary role as an acoustically attenuative backing layer[32]. A 200 nm-thick parylene insulation layer was deposited over the top electrodes and gold wire bonds prior to applying the conductive backing material. It prevents potential short circuits between elements, with minimal changes to impedance characteristics (Supplementary Fig. 12). The resulting EMI shielding further suppressed crosstalk between the TX and RX elements (Fig. 2h, i). The HF crosstalk (Methods) measured at the element was -23.78 dB compared to the -20.69 dB without the backing layer. FEA (Supplementary Fig. 13) shows a theoretical decrease in structural mechanical coupling of 1.8 dB. The larger measured reduction (-3.1 dB) is expected, as the mechanical model excludes voltage conversion losses and electromagnetic (EM) coupling, which accounts for the majority of the crosstalk mitigated by the backing layer's shielding. The baseband inter-element crosstalk noise measured at the ADC (Methods) was reduced on average from 0.64 dBV without the backing layer to −3.88 dBV with the backing layer, reducing electrical artifacts and image noise during operation. This suppression remains effective at higher drive levels (24 V) resulting in an average crosstalk of −3.51 dBV with the backing layer, slightly higher than at 18 V but still substantially lower than the 18 V condition without the backing layer. This improvement is seen in the corner elements as shown in the white dotted box (Supplementary Fig. 14).

In vitro phantom characterization

In order to evaluate the imaging performance of our corner-gap offset array with backing layer, we first assessed the volumetric resolution in vitro. A custom gelatin phantom (Supplementary Fig. 15) containing 250 µm spherical targets[12] was used to measure the PSF along the axial, lateral, and elevational dimensions. The addition of the compliant, gold-wire-compatible backing layer improved the −6 dB PSF width by ~200 µm axially and by ~70 µm across varying depths in the lateral and elevational dimensions (Fig. 3a, Supplementary Fig. 16). These results confirm that the flowable backing layer effectively suppresses reverberation artifacts without compromising element integrity.

Imaging was then performed on a multi-purpose, multi-tissue ultrasound phantom (Model 040GSE, Computerized Imaging Reference Systems Inc.) (Supplementary Fig. 17) to evaluate FOV, depth penetration, and contrast performance (Fig. 3b–d). Using an 18 V drive, the system achieved deep imaging with wire targets visible beyond 9 cm and a wide FOV of approximately 57°, while the incorporation of the flowable backing layer simultaneously reduced EMI, particularly in the near-field region (Fig. 3b). This enabled clear visualization of shallow targets without the need for post-processing noise subtraction, thereby extending the effective imaging range toward the transducer surface.

Imaging of the resolution targets (Supplementary Fig. 18) demonstrated noise reduction and improved delineation of closely spaced targets after incorporating the flowable backing layer (Fig. 3c). Additionally, imaging of the grayscale contrast targets confirmed that both hyperechoic (+3 to +15 dB) and hypoechoic (−3 to −9 dB) regions were clearly distinguished, demonstrating stable gain and dynamic-range uniformity (Fig. 3d). The backing layer consistently improved sharpness and reduced image noise across contrast levels, most notably enhancing hypoechoic visibility in the −9 dB target. The combination of the backing layer and the corner-gap offset array design enables stable imaging at higher transmit voltages. This is particularly important given the sparse array architecture, the 300 µm element pitch and large average impedance (3.72 kΩ at 3.75 MHz) in the current device, where higher operating voltages improve image contrast and penetration depth (Supplementary Fig. 19).

3D aberration-correction beamformer

Conventional beamformers assume a uniform SoS across the imaging medium and compute delay profiles accordingly to reconstruct each pixel from received waveforms. In biological tissue, however, acoustic heterogeneity leads to spatially varying propagation velocities that cause spatial misalignment and image defocusing[33]. In the breast, this effect is particularly pronounced due to the superficial adipose layer, where the SoS (~1400 m s^{-1}) is substantially lower than that of glandular and fibrous tissue (~1500 m s^{-1})[34]. To enhance focusing performance in the breast, we implemented LACR, an aberration-correction beamformer that dynamically compensates for local propagation-velocity variations. The planar 2D geometry of the box array minimizes tissue deformation during scanning[12]. This effect, along with the breast's anatomy, allows the imaging volume to be approximated as a stack of very thin depth layers, each characterized by a locally constant SoS. This layered SoS model simplifies beamforming (Fig. 3e) by reducing the parameter space while capturing the dominant acoustic heterogeneity contributed by the fat layer. Moreover, it enables efficient delay computation by projecting rays through discrete SoS layers rather than integrating along voxel-wise 3D trajectories. This approach improves focusing accuracy with minimal computational overhead compared to traditional grid-based SoS correction methods[33,35,36] which are not scalable to 3D imaging. Using a fixed SoS map, our layered beamformer attains image reconstruction and rendering rates of up to 4 fps, comparable to the performance reported by Marcus et al.[12] for delay-and-sum (DAS) and delay-multiply-and-sum (DMAS) implementations.

LACR utilizes the layered model 3D beamformer (Fig. 3e) to minimize phase error[35] across symmetric 2D subapertures to estimate the optimal SoS in each thickness layer (Fig. 3f, Supplementary Fig. 20). The layered formulation also transforms the otherwise high-dimensional, interdependent 3D multiparameter optimization into a sequential layer-wise process, where the estimated SoS for one layer constrains the next, reducing computational complexity and dependence on initialization values. We first validated the efficacy of the

algorithm and benchmarked it using synthetic aperture focusing radiofrequency (RF) data from Simson et al.[37] and by implementing a 2D variant of LACR to process this dataset (Supplementary Fig. 21, Supplementary Table 3). The estimated SoS achieved a maximum average error of approximately 20 m s^{-1} for both homogeneous and two-layer phantoms, demonstrating accurate SoS estimation and effective separation of the fat and tissue layers (Supplementary Fig. 22).

3D LACR is evaluated using aberrating phantoms (Supplementary Figs. 23,24, Methods) with a superficial fatty layer and is compared against a conventional DMAS beamformer. The PSFs (Fig. 3g, Supplementary Figs. 25,26) show improved spatial accuracy, sharper focusing and reduced sidelobe levels when reconstructed using the derived SoS maps (Supplementary Figs. 27,28) from LACR. Quantitative analysis on custom two-layer gelatin phantoms revealed improvements of up to 60 μm in axial, 150 μm in lateral, and 70 μm in elevational (measured as -6 dB full-width-at-half-maximum). We observed reduced localization error compared with DMAS, confirming effective aberration correction. For the target at 5.0 cm depth, the reconstructed position improved from 5.3 cm without correction to 5.1 cm with LACR. Similarly, the shallower 2.0 cm target, originally mislocalized at 2.2 cm, was accurately resolved at 2.0 cm after applying LACR. The derived SoS map also provides a qualitative indication of local tissue composition (Supplementary Figs. 29, 30), with speed variations reflecting expected contrasts between adipose, fibroglandular and breast implant regions. Computational profiling on an NVIDIA RTX 5070 demonstrated an end-to-end throughput of ~0.1 μs per voxel-candidate. While optimization at a 250 μm voxel size required ~2.15 s per 2 mm slab, coarsening the search grid to 500 μm further reduced the optimization time to as low as 0.40 s per slab. While state-of-the-art 2D differentiable frameworks[37] provide dense speed-of-sound maps, their reliance on the large memory buffers of processors like the RTX A6000 (48 GB memory) and multi-minute runtimes (~300 s/frame) limits their scalability to complex 3D imaging. Our approach trades spatial flexibility for volumetric feasibility, achieving effective aberration correction of the breast in under 55 s on a cost-effective RTX 5070 with lighter memory (12 GB) and workload scope. To the best of our knowledge, this work is the first to implement aberration-correction beamforming in a real-time, wide-angle 3D ultrasound imaging system.

Comparative in vitro evaluation of 2D HHUS and 3D PURE

To compare the ability of 2D HHUS and the 3D PURE system to detect sparsely distributed targets, we conducted a user study using two identically shaped breast phantoms (Supplementary Fig. 31). Each phantom contained multiple point targets (five and six solder spheres for each, ~250 μm diameter) embedded at random locations. For each participant, the phantom used for the 2D and 3D trials was alternated to eliminate bias due to individual target placements. Figure 4a illustrates the study setup: the left image shows participants scanning the phantom using the 3D PURE system, while the schematic on the right highlights the distribution of embedded micro-targets inside the phantom.

Consistent with the known challenges of freehand 2D scanning, where variations in probe pressure, angle, and sweep trajectory often result in gaps in anatomical coverage, the 2D HHUS frequently failed to capture all embedded targets. When the probe was positioned nominally at the correct location, subtle tilting of the probe resulted in complete omission of one target in both viewing angles, and only one reflector was detected even when the 2D imaging plane intersected the region of interest (Fig. 4b). In contrast, the 3D PURE system acquired a wide-angle 3D image from a single placement and consistently captured both targets across viewing angles, demonstrating improved robustness to probe orientation and breast deformation. These results reinforce the inherent limitations of planar, slice-wise imaging for micro-target detection and highlight the advantages of wide-field volumetric acquisition.

Participants identified a significantly greater fraction of targets with 3D PURE than with 2D HHUS (79.7% ± 13.1% vs 60.7% ± 14.9%), corresponding to a mean paired improvement of 19.0 percentage points (paired t-test: $t(9) = 2.781$, $p = 0.0214$; Cohen's $d_z = 0.879$; 95% CI, 3.5 to 34.5 percentage points). Participants also achieved significantly higher detection efficiency with 3D PURE than with 2D HHUS (14.02% ± 2.81% vs 9.58% ± 3.21% of available targets per minute), corresponding to a mean paired improvement of 4.43 percentage points/min ($t(9) = 4.556$, $p = 0.0014$; Cohen's $d_z = 1.441$; 95% CI, 2.23 to 6.64 percentage points/min). Notably, perceived workload, assessed using the NASA-Task Load Index (NASA-TLX) survey[38], was significantly lower overall for the 3D PURE system. The overall Raw TLX (RTLX) score significantly decreased from 11.08 ± 1.99 in 2D HHUS to 7.42 ± 2.96 in 3D PURE ($p = 0.016$). Analyzing the individual subscales (Supplementary Figs. 32, 33) revealed significant reductions for 3D PURE in Mental Demand (11.50 ± 3.21 vs 6.90 ± 3.63, $p = 0.008$), Temporal Demand (11.50 ± 4.22 vs 7.70 ± 4.32, $p = 0.044$), Frustration (12.80 ± 4.29 vs 7.20 ± 4.05, $p = 0.003$), and Effort (median 13.00 vs 6.50, $p = 0.002$). Analysis of Physical Demand (median 9.50 vs 6.50, $p = 0.438$) and Perceived Performance (8.50 ± 3.31 vs 9.10 ± 5.34, $p = 0.769$) resulted in insignificant outcomes. Together, these findings (Fig. 4c) demonstrate that volumetric imaging not only improves detection performance but also significantly reduces the operational burden on users, potentially lowering the reliance on highly trained operators.

In vivo imaging of breast anomalies

We evaluated the system's thermal safety and measured the temperature rise using a thermocouple while the device is on (Supplementary Fig. 34, Methods). We observed only a 1.3 °C temperature rise after 30 min of continuous operation, which is within the FDA's permissible limit[39]. Supported by radiologists, we evaluated the 3D PURE across a diverse set of breast phenotypes to assess its ability to visualize clinically relevant structures in vivo.

We first imaged a subject with round punctate calcifications and were able to visualize these microcalcifications using both the clinical reference system (2D HHUS) and our 3D PURE system (Fig. 4d.i). 3D PURE could detect not only the calcifications detected from 2D HHUS (white dotted circle), but also the other calcifications due to its wide 3D FOV (red dotted circle). A benign cyst was then imaged, and the 3D PURE system clearly depicted the expected hypoechoic morphology (Fig. 4d.ii). In a subject with a retropectoral implant, the 3D PURE system simultaneously resolved the implant boundary and an adjacent cyst (Fig. 4d.iii). Dense fibrous tissue was also readily identified with the 3D PURE system (Fig. 4d.iv). Finally, a solid breast mass (fibroadenoma) was imaged and its margins delineated using both systems, with the 3D PURE system providing volumetric visualization that improved interpretation of the cyst's spatial extent (Fig. 4d.v).

These in vivo demonstrations interpreted by radiologists show that our 3D PURE system can visualize a broad range of clinically relevant structures, including calcifications, cysts, implants, fibrous tissues, and solid masses within a large volumetric FOV.

Vision interface for longitudinal self-breast monitoring

Regular longitudinal monitoring of breast anomalies is beneficial for characterizing disease behavior over time, and essential for monitoring treatment response in settings such as neoadjuvant therapy where repeated, radiation-free evaluation can guide adaptive clinical decision-making[40]. However, for monitoring with portable ultrasound devices, consistently locating the probe on the same anatomical region across sessions is challenging, as ultrasound imaging is highly operator-dependent in typical clinical settings.

https://doi.org/10.1038/s41467-026-74708-3

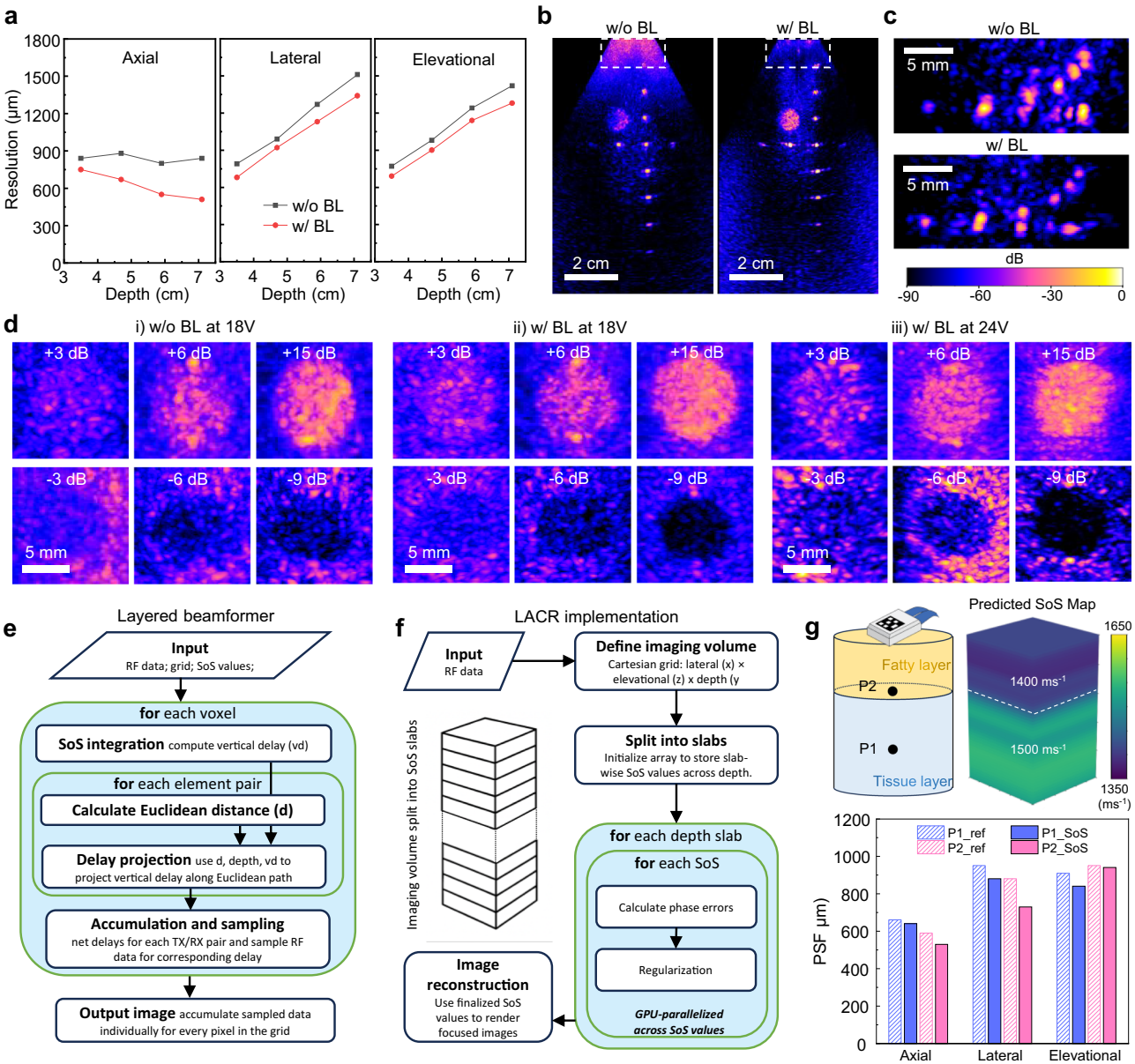

Fig. 3 | Imaging performance of the ultrasound array and layered aberration-correction reconstruction (LACR). a PSF resolution measurements in the axial, lateral, and elevational dimensions from in vitro imaging of 250 μm spherical targets embedded in a custom gelatin phantom. Black lines indicate results w/o the BL, and red lines indicate results w/ the BL. Across depths of 4.1, 5.3, 6.6, and 7.7 cm, the −6 dB PSF widths (axial/lateral/elevational, in μm) were 840/790/770, 880/990/980, 800/1270/1240, and 840/1510/1420 without the backing layer, and 750/680/690, 670/920/910, 550/1130/1140, and 510/1350/1280 with the backing layer, respectively. **b** Ultrasound images acquired on the wire phantom demonstrating 9 cm imaging depth and a 57° FOV. The left image was acquired w/o the BL with a CNR of 6.71 dB in the near field, and the bottom-right image w/ the BL has a CNR of 9.82 dB showing quantitative improvement in image quality. Near-field regions are highlighted with white dotted boxes. **c** Corresponding ultrasound images of the resolution targets in the wire phantom at a depth of 30 mm. The top image was acquired w/o the BL with a CNR of 5.73 dB, and the bottom image w/ the BL and a CNR of 8.32 dB. Color scale for the ultrasound images is shown at the bottom, and the indicated scale is consistently applied across all ultrasound images throughout the manuscript. **d** Ultrasound images of the grayscale group at 3 cm depth, featuring hyperechoic targets (+3, +6, and +15 dB) and hypoechoic targets (−3, −6, and −9 dB), captured i) w/o the BL at 18 V, and ii) w/ the backing layer at 18 V and iii) at 24 V. **e** Flowchart depicting the core layered beamformer. **f** Flowchart depicting the 3D LACR workflow, where the layered beamformer is leveraged for the intermediate calculation of phase errors, estimation of the speed-of-sound (SoS) and the generation of the final image from the radio frequency (RF) data. The layer wise SoS estimation and the reconstruction have been parallelized on a graphical processing unit (GPU). **g** Schematic of the two-point reflectors in the two-layer aberrating phantoms with fatty layer and tissue layer (top left) and the corresponding predicted SoS map (top right) along with the color scale. Corresponding PSF resolutions in the three axes w/ (ref) and w/o (SoS) LACR are plotted at the bottom. Scale bars: 2 cm (**b**), 5 mm (**c**), and 5 mm (**d**).

MyFUS, a computer vision–based solution uses a graphical user interface (GUI) consisting of four panels (Fig. 5b): (i) a control panel guiding the procedure, (ii) a status panel displaying overlap percentages and stored masks, (iii) an instruction panel indicating the current step, and (iv) a live screen showing the real-time body and probe alignment. All processing, visualization overlays, and user feedback (e.g., “move forward/backward”) are performed in real-time using OpenCV graphical functions (Methods). With the user-friendly interface, MyFUS enables patients to reliably recapture a pre-identified anomaly for longitudinal monitoring by repositioning the ultrasound probe to the prior anatomical location (Fig. 5b, Methods).

https://doi.org/10.1038/s41467-026-74708-3

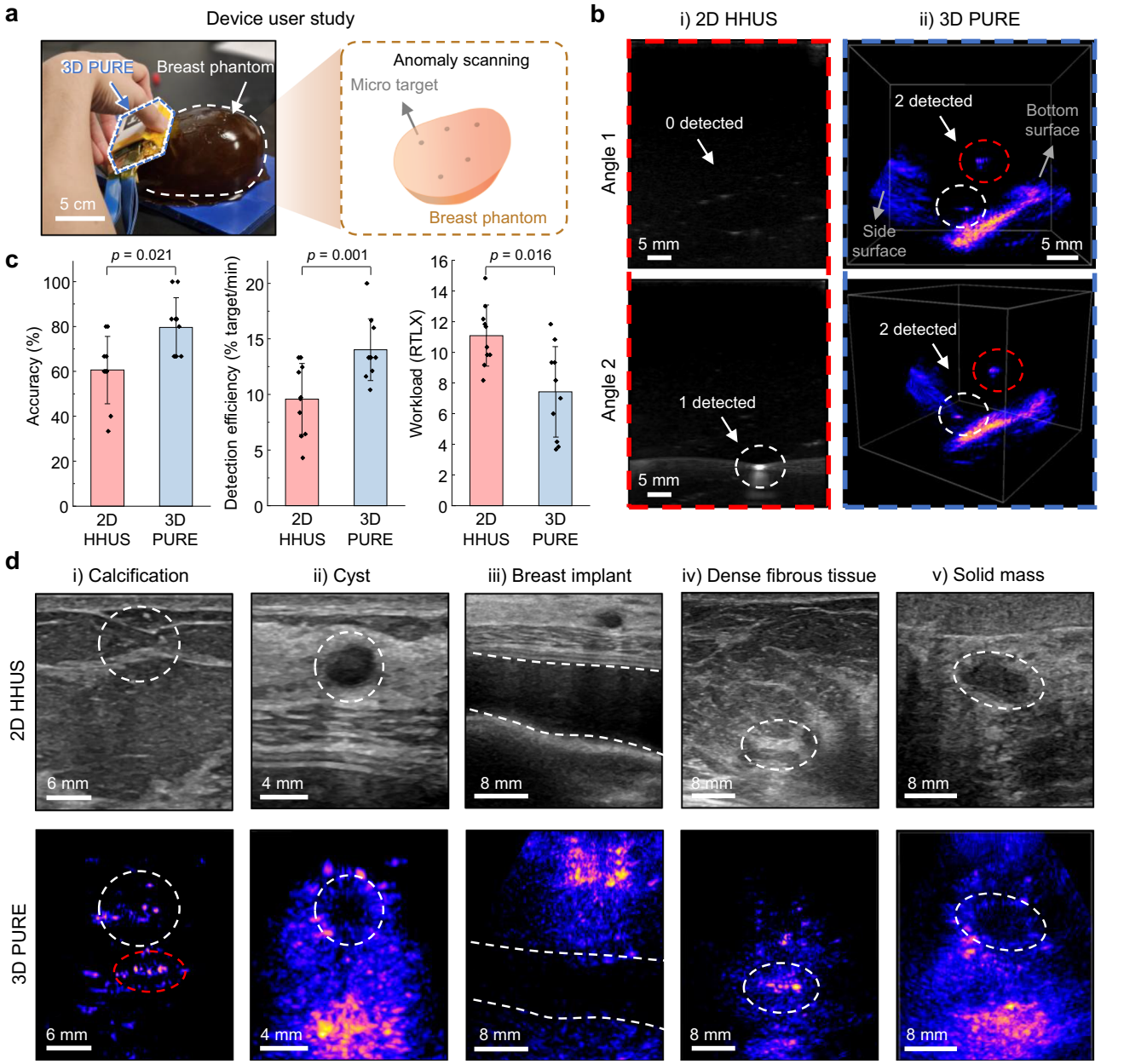

Fig. 4 | Target identification user study and in vivo ultrasound imaging with 3D PURE. a Target identification user study comparing the performance between 2D HHUS and 3D PURE for micro target detection. **b** Ultrasound images from **b.i** 2D HHUS and **b.ii** 3D PURE for detecting two micro targets at the same location with different angles. **c** Result of the user study ($n = 10$, users) about **c.i** accuracy of the number of target findings (2D efficiency: 60.67 ± 14.89% targets detected; 3D efficiency: 79.67 ± 13.10% targets detected), **c.ii** efficiency of detecting targets (2D efficiency: 9.58 ± 3.21% of available targets/min; 3D efficiency: 14.02 ± 2.81% of available targets/min), and **c.iii** workload measured with NASA TLX questionnaire (2D workload: 11.08 ± 1.99%; 3D workload: 7.42 ± 2.96%). **d** In vivo ultrasound images from 2D HHUS and 3D PURE of various kinds of phenotypes including **d.i** calcifications (CNR of 6.61 dB with 2D HHUS and 9.09 dB with 3D PURE), **d.ii** cyst (CNR of 8.45 dB with 2D HHUS and 7.41 dB with 3D PURE), **d.iii** breast implant (CNR of 9.84 dB with 2D HHUS and 6.24 dB with 3D PURE), **d.iv** dense fibrous tissue (CNR of 7.75 dB with 2D HHUS and 9.82 dB with 3D PURE), and **d.v** solid mass (CNR of 8.07 dB with 2D HHUS and 6.17 dB with 3D PURE). Scale bars: 5 cm (**a**), 5 mm (**b**), 6 mm (**d.i**), 4 mm (**d.ii**), 8 mm (**d.iii**–**v**).

An in vivo feasibility trial was conducted with three female and three male subjects, monitoring the breast (Fig. 5c) and a blood vessel (Fig. 5d), respectively. Initial scans were performed with assistance from an ultrasound technician to ensure accurate localization. Follow-up scans were then conducted by the subjects themselves using MyFUS. The 3D ultrasound images acquired across two monitoring sessions were compared by utilizing the structural similarity index measure (SSIM) (Fig. 5e, f, Methods)[41]. Lateral and axial overlap between the reference region of interest (ROI) (green box) and the matched ROI (red box) remain high across sessions (Fig. 5g, h, Methods). For longitudinal breast monitoring, a high degree of spatial overlap between each follow-up session and the initial reference was consistently observed, with mean overlap values of 94.10% for the frontal projection and 87.42% for the side projection (Fig. 5i), substantiating the repeatability and reproducibility of MyFUS. Similarly, for blood vessel monitoring, strong agreement across sessions was confirmed, with mean overlap values of 90.5% in the frontal view and 89.67% in the side view (Fig. 5j).

Beyond these targets, MyFUS was further validated across additional internal anatomies, including dense fibrous breast tissue and rib

https://doi.org/10.1038/s41467-026-74708-3

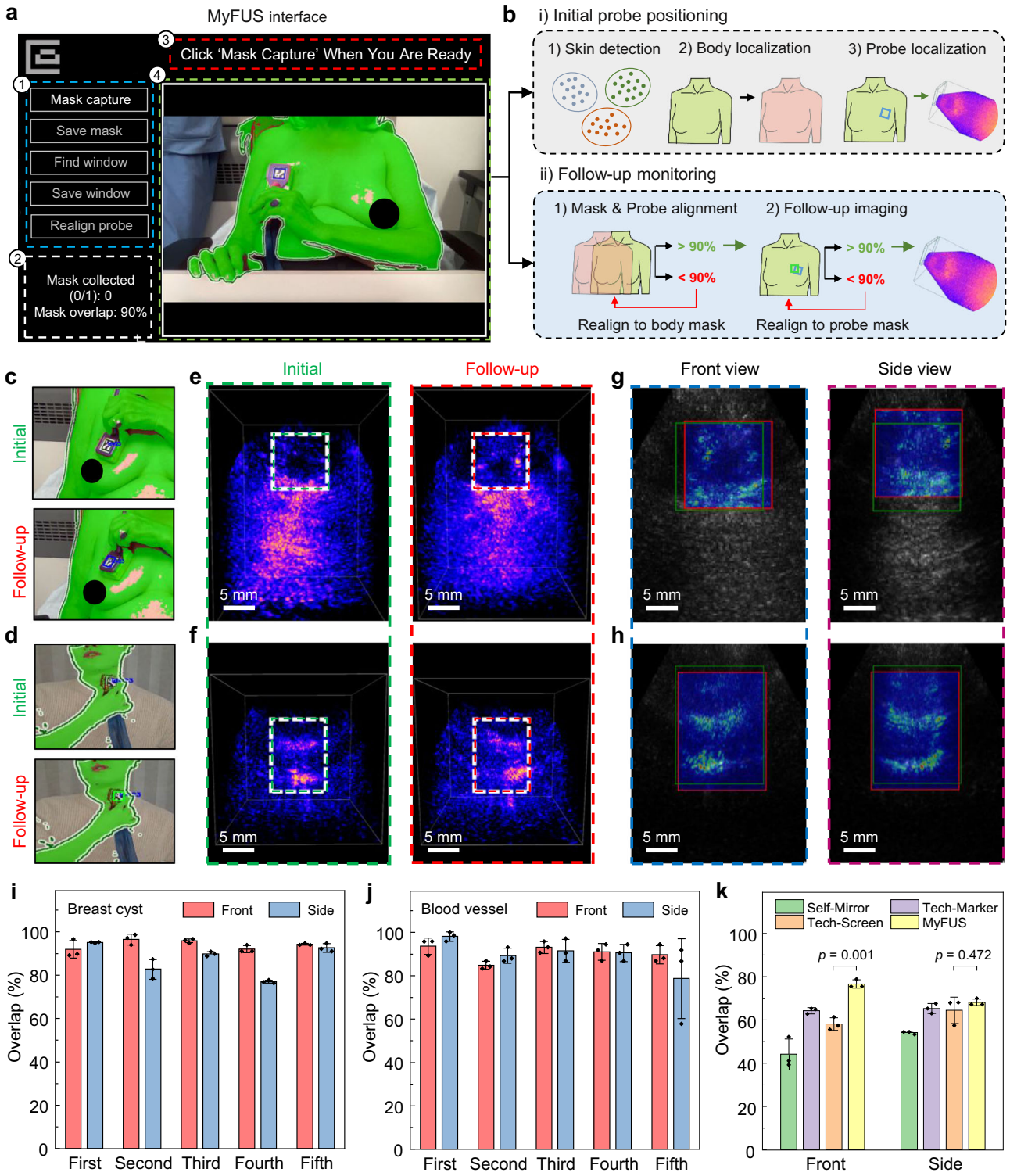

structures, which also exhibited sufficiently high overlap to support reliable longitudinal monitoring (Supplementary Fig. 35). Comprehensive results from the longitudinal human study are summarized in Supplementary Table 4 and Supplementary Figs. 36-39.

We further compared the performance of MyFUS-guided repositioning (MyFUS) with three alternative approaches: (i) self-guided repositioning using a mirror and a skin marker (Self-mirror), (ii) technician-guided repositioning using a skin marker (Tech-marker), and (iii) technician-guided repositioning using real-time ultrasound images (Tech-screen) (Fig. 5k). The MyFUS method yielded the highest area overlap for breast monitoring in the front view: 44.20 ± 5.71%, 64.28 ± 1.12%, 58.10 ± 2.38%, and 76.59 ± 1.63%, and the highest overlap comparable to technician-guided positioning in the side view: 54.12 ± 0.56%, 65.25 ± 1.87%, 64.43 ± 4.95%, and 68.10 ± 1.31%, for Self-mirror, Tech-marker, Tech-screen, and MyFUS, respectively ($n = 3$) (Supplementary Figs. 40-42).

Together, these results demonstrate that the MyFUS interface enables accurate and reliable repositioning of the 3D PURE probehead not only on curved and deformable breast tissue but also on other anatomical locations including the blood vessel under the neck with irregular contours, achieving reproducibility comparable to or better than trained operators. To the best of our knowledge, this is the first

Fig. 5 | Vision interface for repetitive and longitudinal breast monitoring. a A captured image of the vision interface, Mirror my FirstUltraSound (MyFUS), graphical user interface (GUI) operated by a patient: **a.i** Control panel for MyFUS operation. Illuminated buttons (blue dotted line) guide the user through each step. **a.ii** Status panel (white dotted line) displaying real-time body overlap percentage to assist the user in aligning their body with the template mask. **a.iii** Instruction panel (red dotted line) providing the next step in the operation process. **a.iv** Live-view screen (green dotted line) used by the patient for positioning the body and the probe. **b** Schematic workflow of the MyFUS vision interface designed for longitudinal and repetitive self-monitoring of the breast. **c** Photographs of the live-view screen during breast monitoring at the first (top) and second (bottom) monitoring sessions. **d** Photographs of the live-view screen during blood vessel monitoring at the first (top) and second (bottom) monitoring sessions. **e** 3D ultrasound images of a breast cyst obtained during the first (left) and second (right) monitoring sessions. **f** 3D ultrasound images of the blood vessel obtained during the first (left) and second (right) monitoring sessions. **g** Projected views of the 3D breast cyst images from the first (grayscale) and second (color) monitoring sessions in front (left) and side (right) views. **h** Projected views of the 3D blood vessel images from the first (grayscale) and second (color) monitoring in front (left) and side (right) views. The green box denotes the reference ROI from the first session, while the red box indicates the detected ROI with the maximum SSIM value between the reference ROI of the first monitoring and the full image of the second monitoring **(g, h)**. Area overlap of projected 3D ultrasound images acquired across five longitudinal monitoring sessions using MyFUS-guided probe repositioning. MyFUS-enabled longitudinal 3D imaging was performed for (**i**) breast cyst; **j** blood vessel ($n = 3$, frames). The mean and standard deviation values corresponding to plots (**i**) and (**j**) are reported in Supplementary Table 4. **k** Comparison of area overlap percentage across four repetitive-monitoring conditions: Self-mirror, Tech-marker, Tech-screen, and MyFUS ($n = 3$, frames). Front view: 44.20 ± 5.71%, 64.28 ± 1.12%, 58.10 ± 2.38%, and 76.59 ± 1.63% from left to right. Side view: 54.12 ± 0.56%, 65.25 ± 1.87%, 64.43 ± 4.95%, and 68.10 ± 1.31% from left to right. Scale bars: 5 mm (**e**–**h**).

quantitative study of user-oriented probe relocation for operator-independent longitudinal breast ultrasound imaging (Supplementary Table 5). This capability highlights the potential of MyFUS to facilitate at-home and operator-independent longitudinal monitoring of breast anomalies.

Discussion

This work presents a portable, real-time 3D ultrasound system that bridges the gap between highly operator-dependent 2D HHUS and resource-intensive 3D ABUS. We use a rigid 2D probe design rather than a flexible one as the platform is designed for handheld screening instead of continuous wear. A rigid form factor maximizes structural reliability and ensures accurate image reconstruction. To achieve 3D imaging in a portable form factor, our previous work used a sparse box-array architecture in which element proximity leads to higher electrical and mechanical crosstalk, causing preamplifier saturation that limits transmission voltage and penetration depth. Our implementation of a corner-gap offset geometry directly addresses this bottleneck, suppressing crosstalk at the corner-most element and enabling stable operation at higher drive voltages (up to 24 V), which leads to improved contrast and imaging depth.

This array optimization is complemented by a flowable W-ZrO_2-filled PU backing layer that significantly damps element ringing, increases bandwidth and provides EMI shielding (-4.5 dB). Furthermore, this flowable material resolves a major array manufacturing bottleneck by allowing the piezoelectric device to be cleanly and efficiently diced prior to simply pouring the backing layer on top, protecting delicate interconnects and circumventing the risks of co-dicing solid layers. The resulting improvements in bandwidth and resolution are critical for clinical use, for example enabling fine specular reflectors such as microcalcifications to be distinguishable.

We also introduce LACR, our advanced adaptive beamforming algorithm that estimates the variations in SoS through tissue depth, improving phase alignment and reconstruction fidelity in 3D ultrasound imaging. It prioritizes the practical recovery (at O(N) complexity) of spatial resolution without the massive computational burden associated with estimating a full 3D SoS map and the downstream 3D beamforming step, each of which scales to $O(N^3)$. While we acknowledge that dense voxel-wise SoS estimators excel at mapping highly localized, non-stratified heterogeneities (e.g., isolated spherical masses), scaling these advanced techniques to a 3D volume exponentially expands the parameter space. By intentionally posing the optimization problem with a layer-wise constraint, LACR trades absolute lateral spatial flexibility for volumetric feasibility. While breast anatomy is inherently heterogeneous, the superficial adipose layer represents the dominant source of phase error. Approximating these macroscopic tissue transitions as depth-dependent layers captures the bulk of the delay errors, providing a highly effective correction without the overhead of fully unconstrained 3D mapping. Our approach demonstrates that reduced-order reconstruction models can effectively enable resolution enhanced imaging on resource-constrained platforms. To further build on this, porting the solver logic directly to the GPU would eliminate host-device communication overhead (Supplementary Fig. 43), significantly reducing the computational latency of the volumetric correction pipeline.

To better understand the effects of 3D imaging on user performance, we conducted a user study which demonstrates that 3D acquisition lowers the likelihood of missing small abnormalities compared to the planar slicing inherent to 2D ultrasound, thereby reducing cognitive burden and improving overall detection accuracy.

Our in vivo trials further support the translational potential of this integrated approach. The system successfully visualized a diverse range of phenotypes, including calcification, cysts, implants, and solid masses in vivo. These demonstrations lay the groundwork for future large-scale clinical evaluation for estimating the sensitivity and specificity of the 3D PURE by providing representative 3D cases that help radiologists understand the clinical features of this new imaging modality.

The high operator dependence of conventional ultrasound is a barrier to its use in decentralized or home-monitoring settings. The MyFUS vision interface transforms longitudinal monitoring from an expert-driven procedure to a self-guided, reproducible process that can be used by novice users. This reproducibility is vital for longitudinal monitoring in limited clinical settings, to regularly track the growth of an anomaly or the response of a tumor to therapies without visiting clinics. The ability to capture images aligned with initial scans (achieving > 90% projectional lateral image overlap for the breast in both front and side view) suggests that 3D PURE used with MyFUS could serve as a powerful tool for reproducible operator-independent monitoring.

While our prior work[12] established the feasibility of a general portable architecture, translating 3D ultrasound to the rigorous demands of breast tissue imaging required overcoming the inherent contrast deficits of sparse arrays and the clinical hurdle of operator dependence. The innovations introduced here were essential to meet these challenges, namely the corner-gap offset to safely enable higher drive voltages, the pourable backing layer for efficient manufacturing and broader bandwidth, the LACR beamformer to correct tissue heterogeneity, and the MyFUS interface to standardize localization. Rather than being system-specific updates, these represent generalizable strategies that the broader ultrasound community can adopt to advance array fabrication, aberration correction, and operator-independent longitudinal monitoring across various 3D imaging platforms.

Methods

Fabrication of ultrasound arrays

The piezoelectric material, PMN–PT disks (50 mm diameter, 0.4 mm thickness; TRS Technologies), poled in the thickness direction and coated with Au electrodes, were used as the starting material. The 13.5 × 13.5 mm array footprint was cut from each disk using a laser cutter (F1 Ultra, xTool). The cut PMN–PT piece was inserted into a custom carrier PCB. A thin layer of silver conductive paste (SPI Supplies) was applied to connect the bottom electrode to the PCB ground plane and allowed to cure. Three acoustic matching layers with impedances of 15.24, 7.04, and 3.25 MRayl were sequentially deposited on the bottom surface to provide wideband acoustic coupling and mechanical reinforcement.

In the next step, the array was micromachined from the top side using a femtosecond UV laser system (343 nm, up to 10 W; Light Conversion Carbide) integrated with a precision XY stage (Griffin Motion) and galvo scanner (ScanLab IntelliScan14). This process produced ~40 μm kerf widths. The same laser was used to selectively remove electrode material in the gap region between the edge of the piezoelectric ceramic and the elements, since this metal layer could otherwise cause short circuits with the wire bonding. Total machining time for each array was 3–10 min. After micromachining, each element was wirebonded to the carrier PCB using a standard wedge wire bonder (WestBond 7730). A 200 nm parylene layer was deposited via chemical vapor deposition (Specialty Coating Systems, PDS 2010) to electrically isolate the elements and prevent shorting when the conductive backing layer was applied.

Fabrication of matching layers

To achieve efficient acoustic transmission, we implemented a three-layer ¼λ matching stack to transition the piezoceramic impedance (30 MRayl) to that of human tissue (~1.5 MRayl)[42]. Each layer was formulated as an epoxy-based composite using EPO-TEK 301 (Epoxy Technology Inc.) mixed with W and/or ZrO_2 powders to tune acoustic impedance. The matching layers were prepared with the following impedances, compositions, and thicknesses:

i). First layer: 15.24 MRayl (EPO-TEK:W:ZrO_2 = 1:4.1:1), 158.4 μm;
ii). Second layer: 7.04 MRayl (EPO-TEK:ZrO_2 = 1:1.8), 148.9 μm;
iii). Third layer: 3.25 MRayl (EPO-TEK:ZrO_2 = 1:0.08), 135.6 μm.

The thickness of each layer was controlled using a doctor-blade process, and surfaces were lightly lapped as needed to remove local defects and ensure uniformity.

The biocompatibility of the matching layer is further detailed in Supplementary Note 3, with particular emphasis on its safety for dermal-contact applications.

Characterization of transducer elements

The electrical impedance of the transducer elements of the fabricated array was measured using an impedance analyzer (Agilent E4991A, Agilent Technologies). Two key parameters, resonance frequency (f_r) and antiresonance frequency (f_a), can be obtained from the impedance spectrum. For acoustic testing to obtain the bandwidth, a pulse echo test was performed where transducer elements were excited using a 10 V single square wave and the output was measured using a 2.0 mm needle hydrophone (NH2000, Precision Acoustics) located directly underneath the element under measurement in a water tank. The relative position between the array and the hydrophone was adjusted to achieve the strongest signal. The two-way echo response was captured and displayed on an oscilloscope (PicoScope 5444B), while the frequency domain was calculated by fast Fourier transform (FFT).

Fabrication of backing layer

The backing layer was formulated as a composite of PU resin (VytaFlex™ 30, Smooth-On), W powder (APS 1-5 micron, 99.9%, Thermo Scientific), ZrO_2 powder (5 micron, 99%, Sigma Aldrich), and toluene. First, the ZrO_2 powder and W powder were mixed at a 7.5% of ZrO_2-W weight ratio with a vortex mixer at 3,000 rpm for 1 minute. The mixture of part A and part B (1:1 weight ratio) of the PU resin were mixed with the powder mixture at a 1:13.9 weight ratio. The mixed composite was diluted with toluene, whose weight was half of the PU resin. The composite was diluted with a vortex mixer at 3000 rpm for 2 min. After pouring the diluted composite, it was cured for 24 h.

Characterization of backing layer

The acoustic impedance was calculated with the equation as follows

$$Z = \rho * \nu \tag{1}$$

where Z is the acoustic impedance, ρ is the density, and ν is the SoS of the material. Each sample was sliced into a cylindrical shape having 12.15 mm of the diameter (d) and 1.2 mm of the height (h). The density of each sample was calculated based on the measured weight and its volume. The SoS of each sample was calculated through a pulse echo test (Supplementary Fig. 8). A PZT transducer located under the water tank was actuated with a 10 V single sinusoidal wave at 3.5 MHz and a 2.0 mm hydrophone (NH2000, Precision Acoustics), working as a receiver, located at the top of the water tank above the transducer. The pulse arriving time of the case with (t_1) and without (t_2) the backing layer between the transducer and the hydrophone were measured. The SoS (c) of each sample (c_{sample}) was calculated with the equation as follows

$$c_{sample} = \frac{h_{sample}}{t_2 - \frac{t_1 * c_{water} - h_{sample}}{c_{water}}} \tag{2}$$

where c_{water} is set to be 1481 m s^{-1}.

For the conductivity characterization, composites with varying W and ZrO_2 fractions were cast in cylindrical molds (diameter: 12.15 mm), and sectioned into 1.5 mm-thick discs after the curing. Both faces were sputter-coated with gold using an Au sputter coater (SC7640, Quorum Technologies) at 20 mA and 2.0 kV; at a deposition rate of 8 nm per 60 s, two 60 s passes produced an ~16 nm Au film. The coated discs were then diced into 7.1 × 7.1 mm squares, mounted between two flat brass electrodes (20 × 20 mm), and their two-terminal resistance was measured with a precision LCR meter (E4980A, Keysight).

Calculation of the attenuation coefficient of the backing layer

The attenuation of the backing layer for ultrasound waves was measured using the experimental setup shown in Supplementary Fig. 8. The attenuation coefficient was calculated using the following equations[43] as follows

$$T = \frac{2Z_j}{Z_i + Z_j} \ (i = incident\ medium,\ j = transmission\ medium) \tag{3}$$

$$\alpha = \frac{20}{d} log_{10}\left(\frac{A_{ref} * |T|^2}{A_{backing}}\right) [\mathrm{dB\ mm^{-1}}] \tag{4}$$

where $Z_{backing}$, Z_{ref}, T, α, d, $A_{backing}$, A_{ref} denote acoustic impedance of the backing layer, acoustic impedance of the reference medium (water, 1.48 MRayl), pressure transmission coefficient at the water-backing interface, attenuation coefficient, thickness of the backing layer (mm), magnitude of the FFT of the impulse response measured by the hydrophone with the backing layer, and magnitude of the FFT of the impulse response measured by the hydrophone without the backing layer, respectively. The exponent of 2 on the pressure transmission coefficient T accounts for the ultrasound pulse crossing

the water–backing interface twice (once entering, once exiting) during the transmission measurement.

Preparation of gelatin-based tissue-mimicking phantom

The tissue mimicking custom ultrasound phantom was prepared as follows, referring to reported acoustic information of the tissue[44]. Gelatin (Medley Hills Farm) and deionized (DI) water were mixed at a 1:10 ratio and stirred thoroughly by placing the beaker on a hot plate set to 110 °C. Stirring continued until the gelatin was fully dissolved. A 1 cm thick piece of ultrasound-absorbing rubber (Precision Acoustics) was cut and placed at the bottom of a glass beaker. The gelatin solution was then poured into the beaker and cooled in a refrigerator until gelatinized.

A 250 μm tin solder ball was placed at the center of the gelatin layer, and additional gelatin solution was poured into the beaker. After cooling to gelatinize this layer, a second solder ball was placed directly on top of the first ball. This process was repeated, adding solder balls separated by approximately 1 cm of gelatin matrix, until a total of five solder balls were in place. The remaining space in the beaker was filled with the gelatin solution, and the entire beaker was cooled to complete the fabrication of the phantom. The complete fabrication process can be found in our recent report[12].

Preparation of gelatin–oil emulsion gel

A gelatin–oil emulsion gel was formulated using gelatin, medium-chain triglyceride (MCT) oil, DI water, and polysorbate-80 (Tween-80) as a non-ionic surfactant. For a single batch (total volume ≈175 mL), the formulation comprised 113.75 g MCT oil, 12.25 g gelatin, 47.78 g DI water, and 1.5 mL Tween-80. This composition was selected to yield a mechanically stable, acoustically soft emulgel with a target longitudinal sound speed of approximately 1400 m s^{-1} at room temperature.

The aqueous phase was prepared by heating DI water to 75 °C, followed by gradual addition of gelatin under continuous stirring until complete dissolution. Tween-80 was then introduced into the warm gelatin solution and mixed thoroughly to ensure uniform emulsifier dispersion. In parallel, the MCT oil phase was preheated to 75 °C to minimize thermal mismatch during emulsification. The oil phase was subsequently added dropwise to the aqueous phase under highshear mixing to generate a homogeneous oil-in-water emulsion. The resulting emulsion was poured into molds, allowed to cool to room temperature, and then refrigerated to induce gelation.

For layered breast phantoms, a 10 wt% gelatin hydrogel was first cast to represent glandular tissue, followed by deposition of the gelatin–oil emulgel as the superficial adipose-mimicking layer (Supplementary Fig. 23). For PSF characterization, homogeneous 10 wt% gelatin phantoms were used (Supplementary Fig. 15).

In vitro acoustic imaging on phantoms

The imaging performance of the sparse array and cDAQ system was evaluated on three types of phantoms: i) a multipurpose, multi-tissue ultrasound wire phantom (model 040GSE Computerized Imaging Reference Systems Inc.), ii) two custom fabricated two-layer phantoms with a gelatin layer and a gelatin-oil emulsion gel layer, and iii) a custom fabricated gelatin phantom. For better acoustic coupling, either ultrasound gel (Aquasonic 100 Ultrasound Transmission Gel, Parker Laboratories Inc.) or DI water was used.

Crosstalk in the imaging system

Crosstalk was quantified at the preamplifier input and at the post-demodulation baseband output to assess both high-frequency leakage and its contribution to image noise. Unlike standard component-level nearest-neighbor evaluations, this dual-stage approach was selected to capture the end-to-end electromagnetic and acoustic leakage characteristic of the fully integrated system. To measure worst-case coupling, the analog waveform from the corner-most receive element, which inherently experiences the highest transmit–receive leakage, was recorded using a PicoScope 5444B while each transmit element was excited sequentially with a broadband chirp. This measurement provided a direct estimate of high-frequency coupling prior to any conditioning or demodulation. High-frequency (HF) crosstalk was expressed as the power ratio between the received leakage and the transmitted drive amplitude, reported as

$$HF\ crosstalk(dB) = 10log(Prx/Ptx) \tag{5}$$

where peak voltage and device impedance were used to compute the power ratio. Following in-phase/quadrature demodulation, baseband signals from the ADC were collected for all receive channels while each transmit element was pulsed in sequence. Because the ADC output reflects the noise that propagates into beamformed images, the RMS magnitude of each demodulated waveform was computed as a direct measure of residual EMI and cross-channel leakage at the image-formation stage. The resulting baseband crosstalk noise was reported as

$$Baseband\ crosstalk\ noise(dBV) = 20log(Vrms) \tag{6}$$

representing the absolute magnitude of residual crosstalk that contributes to background noise in reconstructed images. This combined analysis characterized high-frequency leakage at the preamplifier stage and its impact on the noise floor observed at the ADC.

3D LACR

Volumetric image reconstruction was performed using a GPU-accelerated frequency-domain beamforming pipeline configured for DAS. The imaging system utilized a sparse 2D "box" array geometry comprising 32 transmit and 32 receive elements per arm with a 300 μm pitch. Synthetic aperture-based 3D image reconstruction was performed on a 5 × 3 × 3 cm^3 3D Cartesian grid with user-defined extents and an isotropic voxel spacing of 250 μm. To suppress sidelobes and artifacts, a Hanning window was applied for temporal apodization and a Hamming window for spatial apodization. The beamformer also incorporated an empirical receive channel timing correction of 250 ns. Data was acquired from two two-layered phantoms using a transmit frequency range of 3–7 MHz, with the resulting in-phase and quadrature (IQ) data saved for subsequent LACR experiments.

To estimate the optimal SoS, we implemented a phase-error sensing metric based on 2D sub-aperture correlation. Transmit and receive masks were constructed as symmetric 1D vectors by duplicating contiguous half-aperture patterns to form full-aperture pairs. Specifically, we tested six sub-aperture pair configurations spanning full/near-full apertures and progressively restricted apertures, implemented either by edge-cropping the active elements or by inserting a center notch, with symmetry enforced by mirroring the half-aperture pattern across the array. These masks were processed using a multi-mask batch interface, allowing non-redundant paired sub-aperture volumes to be beamformed jointly in a single GPU pass.

For each SoS candidate, the beamformer generated two complex volumetric outputs which were used to compute a voxel-wise complex cross-correlation. To ensure robustness against noise, a coherence-based gating mechanism was employed using a 3 × 3 × 3 uniform box filter. Voxels exhibiting coherence values below a threshold of 0.9 were excluded from the error estimation. Across the sub-aperture pairs, we employed a weighted normalization protocol. First, the phase-error profile for each pair was normalized to the unit interval via min–max scaling. The aggregate error metric was then computed as the weighted mean across all pairs, where the weight for each pair was defined as the product of its valid voxel fraction and mean global coherence. This weighting scheme prioritizes pairs with robust spatial support and

signal integrity, effectively suppressing contributions from configurations affected by the low signal-to-noise ratios or limited overlap inherent to sparse aperture designs.

The algorithm minimized the penalized phase error metric in 2 and 2.5 mm slabs via an explicit grid search over candidate velocities ranging from 1350 m s^{-1} to 1650 m s^{-1} in 10 m s^{-1} increments. The final phase error metric was derived from the mean absolute phase angle of the valid voxels in the gated cross-product which was regularized using a deviation threshold of 10 m s^{-1} and a minimal weight to avoid erroneous outliers. This approach avoided gradient-based optimization in favor of a robust sweep, selecting the candidate that minimized the global phase residual across the volume. To manage computational throughput, the platform utilizes an asynchronous, multi-threaded pipeline that decouples real-time rendering from background optimization. The primary visualization thread uses a slab-wise beamformer with a static SoS map to maintain a frame rate of up to 4 fps. LACR runs on a separate background thread, taking up to 55 seconds to fully resolve an entire aberration-corrected volume.

2D LACR

The RF data from Simson et al. was demodulated to IQ format and downsampled during acquisition. The reconstruction framework incorporated the high-frequency sampling rate and demodulation frequency to ensure phase accuracy during delay calculations. Image reconstruction was performed on a high-resolution 2D Cartesian grid with a depth of 40 mm and an isotropic in-plane pixel resolution of 250 μm. The beamformer operated in a DAS configuration. To suppress sidelobes and temporal artifacts, a Hamming window was applied for spatial apodization across the array elements, and a Hanning window was applied for temporal apodization.

To estimate the optimal SoS at specific depths, we implemented a phase-error sensing metric based on sub-aperture correlation (Supplementary Fig. 21). Transmit and receive sub-apertures were defined using precomputed mask pairs. Each mask activated a narrow contiguous band of 17 active elements within 64-element half-apertures. These sub-apertures were mirrored and laterally shifted across the array (12 distinct shift positions) to generate complementary illumination patterns. This configuration allowed for the probing of phase coherence across varying lateral offsets. For each depth slab (thickness = 0.5 mm), the beamformer generated two complex outputs corresponding to the paired sub-aperture masks which were used to compute a complex cross-correlation product. To ensure robustness against noise, a coherence-based gating mechanism was employed. Pixels exhibiting amplitude-normalized coherence values below a threshold of 0.7 were excluded from the error estimation. The final phase error metric was derived from the mean absolute phase angle of the valid pixels in the cross-correlation product.

The algorithm minimized the penalized phase error metric sequentially from superficial to deep layers using 0.5 mm depth steps. For this 2D implementation, the optimization search space ranged from 1350 m s^{-1} to 1650 m s^{-1} in 10 m s^{-1} increments. We finally applied the smoothness regularization using a deviation threshold of 10 m s^{-1} and a minimal weight of 0.00075 to avoid erroneous outliers and generate the final SoS map which were evaluated against the ground truths (Supplementary Fig. 22) from Simson et al.[37].

Target identification user study design

We conducted a target-identification user study with ten participants using two breast-shaped custom phantoms. Among the ten participants, three had prior research experience with ultrasound systems and seven were complete novices, with none possessing formal clinical training as a sonographer or ultrasound technician. Each phantom was prepared using a gelatin-based mixture, and sub-millimetre solder balls (~250 μm) were randomly embedded during casting to emulate microcalcifications or other extremely small anatomical anomalies (Supplementary Fig. 31). To prevent visual cueing, a small amount of red sienna liqua-gel food dye was added to the gelatin-mixture so that the embedded targets were not visible under ambient lighting. One phantom contained five targets and the other contained six.

To avoid bias arising from target placement, the two phantoms were alternated throughout the study and swapped between the 2D and 3D ultrasound systems. The order in which each participant used the two systems was also counterbalanced. For the 2D condition, imaging was performed using a Verasonics Vantage system equipped with an L11-5v linear array transducer. The 2D HHUS system was configured to match the acquisition parameters of the 3D PURE system, resulting in a standardized frame rate of approximately 1.3 fps for both devices. This ensured that detection performance reflected the imaging dimensionality rather than differences in temporal sampling or data update rate.

Participants were instructed to scan each phantom for a minimum of five min. They were asked to scan the full breast volume and identify as many targets as possible. Total scanning time, number of targets correctly identified, and percentage of targets identified were recorded for each trial. After completing each system, participants filled out a NASA-TLX workload questionnaire. Upon completing the second system, participants were provided their first TLX form and asked to complete the second in direct reference to the first. This paired reporting structure enabled consistent scaling across conditions and allowed for systematic comparison of normalized workload scores using min–max normalization.

User study outcomes and NASA-TLX workload analysis

All outcomes were measured within the same participants under both 2D and 3D conditions; analyses were designed for paired/repeated-measures data to control for between-subject variability and maximize power in this sample size ($n = 10$). Descriptive statistics were reported as mean ± SD for parametric analyses and median for nonparametric analyses. All statistical tests were two-sided with a significance level of $\alpha = 0.05$. Detection performance was quantified as the fraction of total available targets identified per trial, and detection efficiency as the fraction of available targets identified per minute. Both endpoints were analyzed as paired continuous outcomes. Normality of paired differences was evaluated using the Shapiro-Wilk test; if normal, paired t-tests were used with Cohen's d_z and 95% confidence intervals for mean paired differences; if non-normal, Wilcoxon signed-rank tests were used with rank-biserial correlation as effect size. Robustness was assessed via sensitivity analyses including the exact sign test, and paired permutation test.

Subjective workload was assessed using the NASA-TLX, which measures six dimensions of perceived workload: Mental Demand, Physical Demand, Temporal Demand, Performance, Effort, and Frustration. After completing each scanning task, participants filled out a TLX questionnaire for the system they had just used. Upon completing the second system, they were shown their first completed TLX form and instructed to score the second in direct reference to the first. This paired rating procedure ensured internal consistency within each participant and reduced variability caused by differences in individual scoring habits.

For statistical analysis, the six TLX subscales were combined using the standard unweighted approach to compute a raw workload score (RTLX) for each participant under each imaging condition. All statistical analyses were performed using the raw TLX scores. However, to account for individual baseline rating biases when visualizing the data, min-max normalized scores were utilized solely for qualitative visualization. These normalized scores are displayed using violin plots for each TLX dimension (Supplementary Fig. 32), and participant-wise heatmaps were created using anonymized labels (P1, P2, …) to illustrate intra-subject relative rating distributions across systems (Supplementary Fig. 33). TLX endpoints were treated as paired continuous outcomes, with normality

assessed by Shapiro-Wilk, paired t-tests used for normally distributed differences, and Wilcoxon signed-rank tests for non-normal differences.

Temperature measurement

To assess the heat generated by the array and cDAQ system, a miniature type-K thermocouple (Evolution Sensors, bead diameter ~300 µm) was placed on the SONOtrain™ Breast phantom with tumors (GT Simulators, Global Technologies) directly beneath the array. The array was operated continuously at 18 V, and the resulting temperature changes were recorded under several operating conditions (Supplementary Fig. 34). Temperature data were logged using proprietary software (DATAQ Instruments Hardware Manager).

Specification of MyFUS system

MyFUS was implemented in Python (v3.10) using OpenCV (v4.8.0), NumPy (v1.26), and scikit-learn (v1.3) to enable real-time torso and probe positioning using a consumer-grade RGB webcam (Logitech C920, 30 fps). The system was validated with other built-in cameras from commercial laptops including Macbook Pro (13-inch, M1, 2020) and Samsung Galaxy Book (NT750XTZ). The 6 × 6 ARUCO fiducial markers were used for geometric calibration, and pre-computed intrinsic camera parameters were loaded to maintain consistent camera–subject distance. During operation, live frames were mirrored horizontally.

Operation of MyFUS system

For the initial probe positioning, the patient's dominant skin color is automatically detected using a K-means clustering algorithm[45]. The algorithm identifies the most frequent color within the frame and defines a hue range of ± 20 in the hue–saturation–value (HSV) color space. Pixels within this range are highlighted in green in real-time. Once the patient is positioned appropriately, the patient can save a body mask (contour of posture) of their torso and the mask is fixed on the screen. Subsequently, the patient scans the breast and identifies anomalies. After an anomaly is located, the software detects an ARUCO marker[46] attached to the probehead, and the corresponding probe position is saved as a reference marker for future monitoring. For follow-up monitoring, the patient aligns their torso with the previously saved body mask on the screen. The real-time body overlap percentage between the current posture and the stored mask is displayed, and once the overlap exceeds 90%, the patient can proceed to the next step. Probe alignment is then achieved by superimposing the live ARUCO marker onto the saved probe mask, also aiming to achieve the overlap exceeding 90%, implying both positional and angular alignment ensured. Multiple probe masks can be stored to track multiple anomalies.

Target overlap calculation between monitorings with MyFUS

To assess similarity between the initial and follow-up scans, the SSIM was calculated. For SSIM computation, the local SSIM calculation window was fixed at 7 × 7 pixels. Projected front and side views of the 3D images were used for SSIM computation. After cropping the ROI (reference ROI) from the initial monitoring session, the cropped ROI was systematically shifted from left to right and top to bottom across the scanned image from the follow-up monitoring, and the position yielding the maximum SSIM score was identified as the detected ROI. Lateral and axial overlap percentages were then calculated between the reference ROI and the detected ROI.

The statistical analysis was conducted to evaluate differences between independent experimental groups. Quantitative data are reported as mean ± standard deviation (SD), with the number of independent measurements (n) indicated in the corresponding figure captions. To compare group means, we employed an unpaired two-sample t-test with unequal variances (Welch's t-test). This method was selected because it does not assume equal population variances and is therefore appropriate for small sample sizes and independently acquired measurements. All tests were performed as two-tailed comparisons. The t-statistic and corresponding p-value were calculated directly from the raw data. A significance threshold of $\alpha = 0.05$ was used to assess statistical significance. Differences were considered statistically significant when $p < 0.05$. Exact p-values are reported where appropriate. No corrections for multiple comparisons were applied unless otherwise stated, as the number of comparisons was limited and hypothesis-driven. All statistical analyses were performed on independent measurements.

Clinical trial for in vivo phenotype imaging

All in vivo trials of breast tissue imaging with subjects were conducted in accordance with the experimental protocol approved by the Committee on the Use of Humans as Experimental Subjects of the Massachusetts Institute of Technology (MIT) (COUHES, no.2011000271 and no. 2501001520). The participants completed the consent forms, which were informed beforehand. All in vivo clinical trials were conducted at MIT Center for Clinical Trial and Research (CCTR) with one clinical research nurse coordinator of the MIT CCTR and 2D ultrasound imaging was conducted either with the Vantage 256 system (Verasonics Inc.) or with the GE Logiq E10 (GE Healthcare). Scan 11-08 Ultrasound Gel (Parker Laboratories Inc.) was used for acoustic coupling. All observed phenotypes were corroborated by prior medical history, radiology reports, and consultation with a radiologist. Further details of the human study protocol, including inclusion criteria, study procedures, and image interpretation and validation, are provided in Supplementary Note 4.

Contrast-to-Noise Ratio (CNR) calculation

CNR was measured on point targets in a CIRS phantom using paired regions of interest (ROIs) for the target and its local background. Target ROIs were circular, centered on visually identified point targets, with radii selected to capture the point spread without overlapping nearby structures. Background ROIs were either a concentric annulus or an adjacent circle of equal area, placed to avoid spillover, edges, and artifacts. ROIs intersecting phantom boundaries, inhomogeneities, or saturated pixels were redefined.

Intensities were normalized per acquisition to remove global gain or offset differences. No spatial filtering was applied prior to CNR computation. Any gamma or display-only transforms were used solely for figure generation. All statistics were computed in double precision on raw ROI pixels.

Let the mean and standard deviation of the target and background ROIs be denoted as μ_t, σ_t, μ_b, and σ_b, respectively. The pooled noise term was calculated as:

$$\sigma_{rms} = \sqrt{\frac{\sigma_t^2 + \sigma_b^2}{2}} \tag{7}$$

The linear-domain CNR was then defined as:

$$CNR_{lin} = \frac{|\mu_t - \mu_b|}{\sigma_{rms}} \tag{8}$$

Which was converted to decibels as:

$$CNR_{dB} = \log_{10}(CNR_{lin}) \tag{9}$$

For this volumetric data, CNR was calculated on 2D projection images captured from the 3D rendering view. All computations were implemented in Python using vectorized operations, ensuring deterministic results for fixed ROI placements.

Ethics
Every experiment involving animals, human participants, or clinical samples have been carried out following a protocol approved by the Committee on the Use of Humans as Experimental Subjects of the Massachusetts Institute of Technology (MIT) (COUHES, no.2011000271 and no. 2501001520). Each participant gave informed written consent before conducting the human studies.

Reporting summary
Further information on research design is available in the Nature Portfolio Reporting Summary linked to this article.

Data availability
All data supporting the findings of this study are available within the article and its supplementary files. Any additional requests for information can be directed to, and will be fulfilled by, the corresponding authors. Source data are provided with this paper.

Code availability
The full implementation code of MyFUS[47] is provided here: (https://github.com/hyoon970/myFUS). Other codes supporting the findings of this study will be made available upon request to the corresponding authors.

References

1. Kim, J. et al. Global patterns and trends in breast cancer incidence and mortality across 185 countries. *Nat. Med.* **31**, 1154–1162 (2025).
2. Society, A. C. et al. Breast cancer facts & figures 2024–2025 (2024).
3. Checka, C. M., Chun, J. E., Schnabel, F. R., Lee, J. & Toth, H. The relationship of mammographic density and age: implications for breast cancer screening. *Am. J. Roentgenol.* **198**, W292–W295 (2012).
4. Miglioretti, D. L. et al. Radiation-induced breast cancer incidence and mortality from digital mammography screening: a modeling study. *Ann. Intern. Med.* **164**, 205–214 (2016).
5. Giannakou, A., Dagdeviren, C. & Ozmen, T. Conformable ultrasound breast patch-the future of breast cancer screening? *Eur. J. Breast Health* **21**, 90 (2025).
6. Jang, J. Y. et al. Clinical significance of interval changes in breast lesions initially categorized as probably benign on breast ultrasound. *Medicine* **96**, e6415 (2017).
7. Morrow, M., Waters, J. & Morris, E. MRI for breast cancer screening, diagnosis, and treatment. *Lancet* **378**, 1804–1811 (2011).
8. O'Connor, M. K. Molecular breast imaging: an emerging modality for breast cancer screening. *Breast cancer Manag.* **4**, 33–40 (2015).
9. Moore, S. G., Shenoy, P. J., Fanucchi, L., Tumeh, J. W. & Flowers, C. R. Cost-effectiveness of MRI compared to mammography for breast cancer screening in a high risk population. *BMC health Serv. Res.* **9**, 9 (2009).
10. Hruska, C. B. et al. Diagnostic workup and costs of a single supplemental molecular breast imaging screen of mammographically dense breasts. *Am. J. Roentgenol.* **204**, 1345–1353 (2015).
11. Du, W. et al. Conformable ultrasound breast patch for deep tissue scanning and imaging. *Sci. Adv.* **9**, eadh5325 (2023).
12. Marcus, C. et al. Real-time 3D Ultrasound Imaging with an Ultra-Sparse, Low Power Architecture. *Adv. Healthc. Mater.* **15**, e05310 (2026).
13. Yoon, H. et al. Decoding tissue biomechanics using conformable electronic devices. *Nat. Rev. Mater.* **10**, 4–27 (2025).
14. Kim, J.-H., Yoon, H., Viswanath, S. & Dagdeviren, C. Conformable piezoelectric devices and systems for advanced wearable and implantable biomedical applications. *Annu. Rev. Biomed. Eng.* **27**, 255–282 (2025).
15. Zhang, L., Du, W., Kim, J. H., Yu, C. C. & Dagdeviren, C. An emerging era: conformable ultrasound electronics. *Adv. Mater.* **36**, 2307664 (2024).
16. Eisenbrey, J. R., Dave, J. K. & Forsberg, F. Recent technological advancements in breast ultrasound. *Ultrasonics* **70**, 183–190 (2016).
17. Soo, M. S., Baker, J. A. & Rosen, E. L. Sonographic detection and sonographically guided biopsy of breast microcalcifications. *Am. J. Roentgenol.* **180**, 941–948 (2003).
18. Kunitake, J. A. et al. Biomineralogical signatures of breast microcalcifications. *Sci. Adv.* **9**, eade3152 (2023).
19. Boca, I., Ciurea, A. I., Ciortea, C. A. & Dudea, S. M. Pros and cons for automated breast ultrasound (ABUS): a narrative review. *J. personalized Med.* **11**, 703 (2021).
20. Rella, R. et al. Automated breast ultrasonography (ABUS) in the screening and diagnostic setting: indications and practical use. *Academic Radiol.* **25**, 1457–1470 (2018).
21. Li, C., Duric, N., Littrup, P. & Huang, L. In vivo breast sound-speed imaging with ultrasound tomography. *Ultrasound Med. Biol.* **35**, 1615–1628 (2009).
22. Chen, R. et al. PMN-PT single-crystal high-frequency kerfless phased array. *IEEE Trans. Ultrason., Ferroelectr., Frequency Control* **61**, 1033–1041 (2014).
23. Grewe, M. G., Gururaja, T., Shrout, T. R. & Newnham, R. E. Acoustic properties of particle/polymer composites for ultrasonic transducer backing applications. *IEEE Trans. Ultrason., Ferroelectr., frequency control* **37**, 506–514 (2002).
24. Jayakumari, V., Shamsudeen, R., Rajeswari, R. & Mukundan, T. Viscoelastic and acoustic characterization of polyurethane-based acoustic absorber panels for underwater applications. *J. Appl. Polym. Sci.* **136**, 47165 (2019).
25. Hu, H. et al. Stretchable ultrasonic transducer arrays for three-dimensional imaging on complex surfaces. *Sci. Adv.* **4**, eaar3979 (2018).
26. Hu, H. et al. A wearable cardiac ultrasound imager. *Nature* **613**, 667–675 (2023).
27. Genovés, V. et al. Micronized recycle rubber particles modified multifunctional polymer composites: application to ultrasonic materials engineering. *Polymers* **14**, 3614 (2022).
28. Zhang, L. et al. A conformable phased-array ultrasound patch for bladder volume monitoring. *Nat. Electron.* **7**, 77–90 (2024).
29. State, M., Brands, P. J. & van de Vosse, F. N. Improving the thermal dimensional stability of flexible polymer composite backing materials for ultrasound transducers. *Ultrasonics* **50**, 458–466 (2010).
30. Wu, J. et al. A fiber-shaped ultrasonic transducer by designing a flexible epoxy/nano-zirconia composite as an acoustic matching layer. *J. Mater. Chem. B* **13**, 3023–3031 (2025).
31. Kong, F. et al. A wearable ultrasound patch based on ultrathin backing for biomedical imaging. *Sens. Actuators A: Phys.* **393**, 116854 (2025).
32. Orasugh, J. T. & Ray, S. S. Functional and structural facts of effective electromagnetic interference shielding materials: a review. *ACS omega* **8**, 8134–8158 (2023).
33. Rau, R., Schweizer, D., Vishnevskiy, V. & Goksel, O. in *2019 IEEE International Ultrasonics Symposium (IUS)*. 2003-2006 (IEEE).
34. Malik, B., Klock, J., Wiskin, J. & Lenox, M. Objective breast tissue image classification using quantitative transmission ultrasound tomography. *Sci. Rep.* **6**, 38857 (2016).
35. Bezek, C. D. & Goksel, O. Analytical estimation of beamforming speed-of-sound using transmission geometry. *Ultrasonics* **134**, 107069 (2023).
36. Stähli, P., Kuriakose, M., Frenz, M. & Jaeger, M. Improved forward model for quantitative pulse-echo speed-of-sound imaging. *Ultrasonics* **108**, 106168 (2020).

37. Simson, W. et al. in *International Conference on Medical Image Computing and Computer-Assisted Intervention*. 428–437 (Springer).
38. Hart, S. G. & Staveland, L. E. in *Advances in psychology* **52**, 139–183 (Elsevier, 1988).
39. U.S. Food and Drug Administration. Evaluation of thermal effects of medical devices that produce tissue heating and/or cooling: draft guidance for industry and Food and Drug Administration staff. FDA (2024).
40. Hayward, J. H. et al. ACR appropriateness criteria® monitoring response to neoadjuvant systemic therapy for breast cancer: 2022 update. *J. Am. Coll. Radiol.* **20**, S125–S145 (2023).
41. Wang, Z., Bovik, A. C., Sheikh, H. R. & Simoncelli, E. P. Image quality assessment: from error visibility to structural similarity. *IEEE Trans. image Process.* **13**, 600–612 (2004).
42. Zhou, Q., Lam, K. H., Zheng, H., Qiu, W. & Shung, K. K. Piezoelectric single crystal ultrasonic transducers for biomedical applications. *Prog. Mater. Sci.* **66**, 87–111 (2014).
43. Kim, H. et al. High-attenuation backing layer for miniaturized ultrasound imaging transducer. *IEEE Trans. Ultrason. Ferroelectr. Freq. Control* **69**, 1960–1969 (2022).
44. Fernandez, S. V. et al. A dynamic ultrasound phantom with tissue-mimicking mechanical and acoustic properties. *Adv. Sci.* **11**, 2400271 (2024).
45. Lloyd, S. Least squares quantization in PCM. *IEEE Trans. Inf. theory* **28**, 129–137 (1982).
46. Garrido-Jurado, S., Muñoz-Salinas, R., Madrid-Cuevas, F. J. & Marín-Jiménez, M. J. Automatic generation and detection of highly reliable fiducial markers under occlusion. *Pattern Recognit.* **47**, 2280–2292 (2014).
47. Shah, A. et al. MyFUS: Custom software application for Ultrasound Breast Patch longitudinal study (Version 1.0) [Software]. *Zenodo*. https://doi.org/10.5281/zenodo.20531626 (2026).

Acknowledgements

C.D. thanks to her late aunt, F. Caliskanoglu, who lost her life because of breast cancer in 2015, for inspiring this work since then. We thank E. Nguyan for helping in MyFUS development and J. Hou for helping in schematic drawing. We thank T. Urman, Gabriel Varga, from MIT CCTR for assisting in the clinical study. We thank Y. Li, an ultrasound technician from MGH for helping with the in vivo human trials. We also gratefully acknowledge Amanda Nguyen for carrying our ultrasound array payload aboard the first ever all female crew Blue Origin spaceflight mission (*11th spaceflight* under the New Shepard program), enabling the first exposure of this technology to the space environment and symbolizing its potential for future space-based biomedical applications.

Author contributions

C.D. and M.O.G.N. conceptualized the project. C.D., M.O.G.N., S.V., and H.Y. designed the experiments. M.O.G.N., S.V., H.Y. and A.S. fabricated and packaged the ultrasound transducers. H.Y., M.O.G.N., and D.S. designed and fabricated the backing layer. M.O.G.N., H.Y., and S.V. characterized the backing layer. H.Y. and S.V. designed and conducted the FEA simulation. CM performed the virtual aperture simulations. SV proposed and developed the LACR algorithm. M.O.G.N. designed and fabricated the custom gelatin phantoms. M.O.G.N., S.V., and H.Y. performed the in vitro characterization and imaging on phantoms. M.O.G.N., S.V., and H.Y. conducted the target identification user study. C.D., M.O.G.N., S.V., and H.Y. planned the human subject trials. A.S., C.D., M.O.G.N., S.V. and H.Y. performed the in vivo breast tissue imaging. A.S. and H.Y. developed the MyFUS software and H.Y. performed the image analysis. M.O.G.N., S.V., H.Y., A.C., T.O. and C.D. contributed in data analysis and data interpretation. M.O.G.N., S.V. and H.Y. wrote the paper, and all authors contributed to the review and editing. C.D. directed all the research activities and supervised the project.

Funding

This work was supported by NSF CAREER: Conformable Piezoelectrics for Soft Tissue Imaging (grant no. 2044688), NSF CCSS: Conformable Sparse-Array Ultrasound Patch for Wearable 3D Breast Imaging (grant no. 2524831), 3 M Non-Tenured Faculty Award, and The Lyda Hill Foundation and MIT Media Lab Consortium funding. S.V. acknowledges the support from the Tata Center Technology and Design Fellowship administered by the MIT Energy Initiative.

Competing interests

The authors declare no competing interests.

Additional information

Supplementary information The online version contains supplementary material available at https://doi.org/10.1038/s41467-026-74708-3.

Correspondence and requests for materials should be addressed to Canan Dagdeviren.

Peer review information *Nature Communications* thanks Xuecheng He, Tailin Xu, and Syed Muhammad Yousaf Farooq for their contribution to the peer review of this work. A peer review file is available.